JGR Space Physics

RESEARCH ARTICLE
10.1029/2021JA029934

Key Points:

- Pre-sunrise Equatorial Plasma Bubbles (EPBs) remained after sunrise and stayed 3.5 hr during the daytime in the American longitude sector on 18 March 2015
- The plasma bubbles appear to be generated by an effect of disturbance wind dynamo in the recovery phase of the St. Patrick storm in 2015
- The evolution of post-sunrise EPBs exhibits longitudinal dependence between the east coast and west coast of the South America continent

Supporting Information:

Supporting Information may be found in the online version of this article.

Correspondence to:

C. S. Carmo,
carolina.carmo@inpe.br;
carolscarmo25@gmail.com

Citation:

Carmo, C. S., Pi, X., Denardini, C. M., Figueiredo, C. A. O. B., Verkhoglyadova, O. P., & Picanço, G. A. S. (2022). Equatorial plasma bubbles observed at dawn and after sunrise over South America during the 2015 St. Patrick's Day storm. *Journal of Geophysical Research: Space Physics*, *127*, e2021JA029934. https://doi.org/10.1029/2021JA029934

Received 2 SEP 2021
Accepted 14 SEP 2022

Author Contributions:

Conceptualization: C. S. Carmo
Data curation: C. S. Carmo
Formal analysis: C. S. Carmo, X. Pi, O. P. Verkhoglyadova
Investigation: C. S. Carmo, X. Pi
Methodology: C. S. Carmo, C. A. O. B. Figueiredo
Resources: C. S. Carmo, X. Pi
Software: C. S. Carmo
Supervision: X. Pi, C. M. Denardini, C. A. O. B. Figueiredo, O. P. Verkhoglyadova
Validation: C. S. Carmo, C. A. O. B. Figueiredo
Writing – original draft: C. S. Carmo

Equatorial Plasma Bubbles Observed at Dawn and After Sunrise Over South America During the 2015 St. Patrick's Day Storm

C. S. Carmo[1,2], X. Pi[2], C. M. Denardini[1], C. A. O. B. Figueiredo[1], O. P. Verkhoglyadova[2], and G. A. S. Picanço[1]

[1]National Institute for Space Research (INPE), Sao Jose dos Campos, Brazil, [2]Jet Propulsion Laboratory, California Institute of Technology, Pasadena, CA, USA

Abstract This paper presents an analysis of Equatorial Plasma Bubble (EPB) events that occurred during pre- and post-sunrise hours in the South America sector on 18 March 2015, when the St. Patrick's Day geomagnetic storm was in the recovery phase. The data from a set of multi-diagnostic instruments, including Global Navigation Satellite Systems (GNSS) receivers, L-band GNSS ionospheric scintillation monitors, ionosondes, and a Fabry-Perot interferometer, are analyzed. Strong L-band amplitude scintillation was observed with spread-F and total electron content (TEC) fluctuations at times when the electron density and tTEC were minimum with respect to their diurnal variations. The EPBs remained observed for about 3:30 hr after sunrise on the east coast of the South American continent. The daytime ionospheric irregularities show a longitudinal dependency between the west and east coasts, separated by about 3,600 km. Our analysis of the observations suggests that a Disturbance Dynamo Electric Field effect caused by storm-time wind perturbations might have triggered the Rayleigh-Taylor instability near local dawn on the east and west coasts of the South American continent. The effects of ambient ionosphere-thermosphere conditions on the evolution of irregularities are assessed to understand the longitudinal differences. The assessment includes the effect of the *E* region that appears in the morning hours and the effects of geomagnetic declination and tilting the solar-terminator.

1. Introduction

Equatorial Plasma Bubbles (EPBs) over South America have been studied extensively over the years. The EPBs are defined as plasma depletion formed by Rayleigh-Taylor Instability (RTI) processes (Kelley, 2009). Different instruments and methodologies can be used to detect these EPBs, such as Ionosondes (Abdu et al., 2003, 2012), All-Sky Imager (Pimenta et al., 2007; Vargas et al., 2020), total electron content (TEC) (Barros et al., 2018; Silva et al., 2019), Very High Frequency (VHF) radars (Abdu et al., 2009), scintillation index (S4) (De Paula et al., 2007; De Rezende et al., 2007), disturbance ionospheric index (DIX) (Denardini et al., 2020), and Rate Of TEC Index (ROTI) (Carmo et al., 2021; de Jesus et al., 2020). These irregularities are commonly generated after sunset (Abdu et al., 2003; Agyei-Yeboah et al., 2021; Magdaleno et al., 2012; Vargas et al., 2020). There are also studies reporting plasma bubbles occurring post-midnight (Arruda et al., 2006; Otsuka, 2018), and during magnetic storms (Abdu, 2012), while cases of pre-sunrise plasma bubbles are rare (Burke, 1979; Mrak et al., 2021; Sripathi et al., 2018; Wu et al., 2020; Yeh et al., 2001; Zakharenkova et al., 2019).

Sripathi et al. (2018) investigated an unusual generation of EPBs at dawn (until 05:30 LT), in the Indian sector, during a moderate magnetic storm (4–5 February 2011, $K_p = 6$). They attributed the triggering mechanism to a combination of Prompt Penetration Electric Field (PPEF) and Disturbance Dynamo Electric Field (DDEF), despite showing no evidence of these. Mrak et al. (2021) also noted EPB persistence after dawn (2 hr) but did not explain the possible mechanisms that make EPBs persist. Wu et al. (2020) observed an equatorial plasma bubble near sunrise (until 08:00 LT) during the recovery phase of a magnetic storm (6–8 November 2015). They suggested that the enhanced eastward electric field uplifted the *F* layer, triggering the RTI and generating an EPB. But all these events did not last long (hours) after sunrise, which makes the case presented in this study a unique one, where the EPBs lasted about 3:30 hr after sunrise. In addition, this study aims to investigate possible mechanisms by comparing similarities and differences in two longitude sectors separated about 30° for the persistence duration of these irregularities.

Writing – review & editing: C. S. Carmo, X. Pi, C. M. Denardini, C. A. O. B. Figueiredo, O. P. Verkhoglyadova, G. A. S. Picanço

Zakharenkova et al. (2019) studied plasma bubbles during the 2015 St. Patrick's Day magnetic storm within a global overview, and they observed EPBs in the pre-dawn in South America. They suggested that the DDEF was responsible for the generation of these rare EPBs. However, they did not explain the longitudinal characteristics of the plasma bubbles and did not report daytime EPBs. Our observations presented in this work address the dawn- and post-dawn time EPBs. Our analysis aims to study and understand the triggering, development, and longitudinal dependence as well as duration of the dawn- and post-dawn EPBs occurred in the recovery phase of the St. Patrick's Day magnetic storm on 18 March 2015. This study aims to present comprehensive observations of pre- and post-sunrise EPBs in the South American sector using multi-diagnostic observations from different instruments. The uniqueness of this study is our effort to understand the generation and evolution of these EPBs around dawn and daytime and the differences and similarities observed at different longitudes (west and east coasts).

2. Available Datasets and Methodology

In the present study, we use a set of data from multi-diagnostic instruments, including Global Navigation Satellite Systems (GNSS) ground receivers, L-band GNSS ionospheric scintillation monitors, ionosondes, and Fabry-Perot interferometer on the South American sector. GNSS receivers are used for regional and local observations of irregularities seen in TEC. Ionosondes are used to observe the presence of Spread F, which is associated with EPB. A Fabry-Perot interferometer is used to observe wind characteristics. More information about measurements from these instruments is described in Sections 2.1 and 2.2.

Figure 1 shows the station locations from which data are collected and used to analyze ionospheric irregularities in this study. Panel (a) gives the locations and names of stations of special interest (studied in detail), and panel (b) shows the locations of distributed GNSS receivers (blue points) and ionosondes (red triangles), from which GNSS data are processed to produce 2D regional TEC and ROTI maps and ionosonde data are presented to spread-F activity. The continuous red line in panel (b) across the map indicates the geomagnetic equator.

Table 1 contains information about eight specific GNSS receivers, including latitude, longitude, dip angle, and time of sunrise.

The data access information for Table 1 is presented in the Acknowledgments, Samples, and Data section.

2.1. GNSS, TEC, and ROTI Calculation

Observables of GNSS signals are processed to generate Global Positioning System (GPS) TEC maps and ROTI maps, which are used to detect plasma depletions (e.g., EPB) and ionospheric irregularities.

TEC above each station was obtained by processing GPS RINEX data using a GPS-TEC Software Program (Seemala & Valladares, 2011, version 3.0). The program uses GPS navigation data and the satellite biases from Differential Code Bias (DCB) IGS data. Moreover, the software calculates the receiver biases and computes the slant TEC (STEC) and the vertical TEC (VTEC). These parameters are given in TEC units (TECU = 10^{16} electrons/m^2). In addition, data at elevation angles lower than 30° is excluded to avoid noisy data such as multipath errors at low elevation angles.

We also use the ROTI defined in Pi et al. (1997, 2013) using GPS and GLONASS constellations data. To calculate the ROTI, the STEC is obtained using only the carrier-phase, that is,

$$\mathrm{STEC} = \left(\frac{L_1}{f_1} - \frac{L_2}{f_2}\right) \frac{f_1^2 f_2^2}{f_1^2 - f_2^2} \frac{c}{K}, \tag{1}$$

where c is the speed of light in the vacuum, and the parameter K is 40.3 m^3/s^2, as presented in Cherniak et al. (2018). For GPS, the carrier frequencies f_1 and f_2 are 1,575.42 and 1,227.60 MHz, respectively. For GLONASS, the frequencies f_1 and f_2 are 1,602.0 MHz + 0.5625 * R and 1,246.0 MHz + 0.4375E6 * R, respectively, where R is the reference channel (the correspondent number for each Pseudorandom Noise [PRN], https://www.glonass-iac.ru/en/GLONASS). At last, L_1 and L_2 are the phase measurements corresponding to f_1 and f_2, respectively.

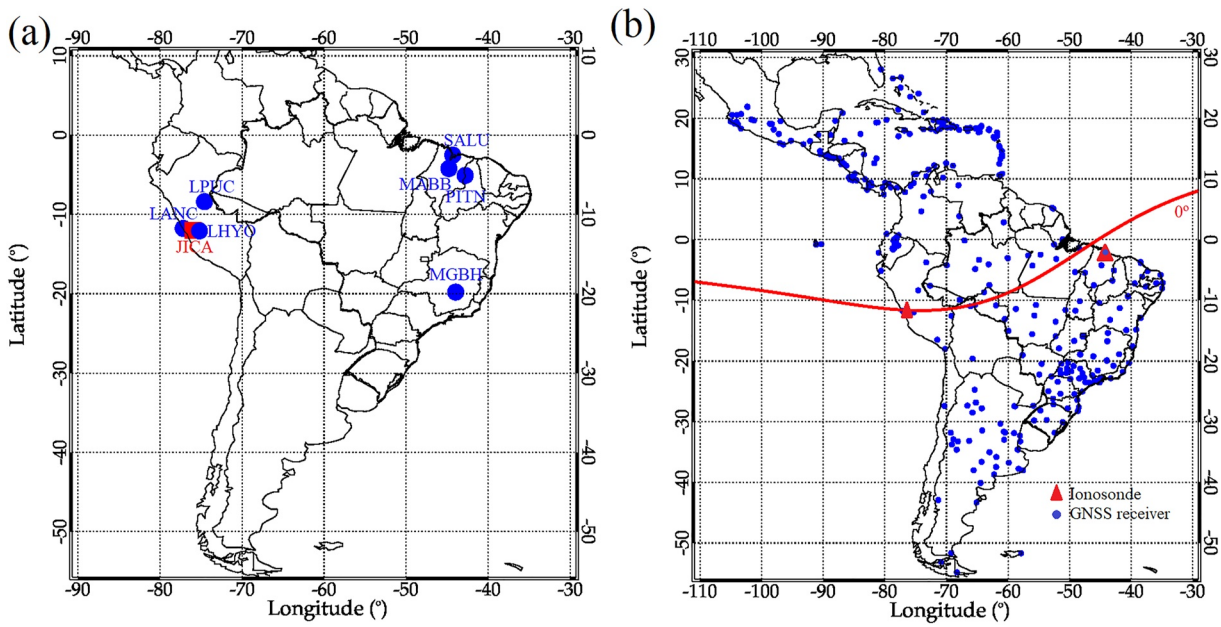

Figure 1. Maps showing the locations of the stations from which data are collected and analyzed to study the ionospheric irregularities. Panel (a) gives the locations and names of stations where data are analyzed in detail. Panel (b) shows the geographic locations of distributed instruments used in this study. The geomagnetic equator is indicated using a red line across the map in panel (b), with the marks of GNSS receivers (blue points) and ionosondes (red triangles). Additionally, a Fabry-Perot interferometer placed in Jicamarca (red square, panel a) is also used in this study.

The Rate Of TEC (ROT) is calculated by the difference between the consecutive sTEC data samples, and the difference is then divided by the time interval. The ROT is calculated using Equation 2 (Pi et al., 1997, 2013).

$$\mathrm{ROT} = \frac{\mathrm{sTEC}_k^i - \mathrm{sTEC}_{k-1}^i}{t_k - t_{k-1}}, \tag{2}$$

where i corresponds to a specific PRN of a given GNSS satellite, k is the epoch time, and $k-1$ is the previous epoch. Using sTEC instead of vTEC for ROT calculation concerns the following factors: (a) using sTEC measurements does not require dealing with slant-to-vertical mapping, which introduces errors at low elevation angles, while using vTEC does; (b) using sTEC does not require removing satellite and receiver instrumental interfrequency biases, which makes it difficult when applying the algorithm to data from globally distributed thousands of stations or receivers, while using vTEC does. The slight difference between the two radio paths of the consecutive sTEC samples can cause a small geometric effect, which makes sTEC slightly larger at lower elevation angles. This effect is removed by detrending ROT. In the present work, we calculate detrended ROT for every 30-s.

Table 1
Latitude, Longitude, Dip Angle, and Time of Sunrise of the Global Navigation Satellite System Stations Used in This Study

Station	Latitude (°)	Longitude (°)	Dip (°)	Declination (°)	Sunrise (LT)	Sunrise (UT)
1-Ancon (LANC)	−11.77	−77.17	0.1	−1.45	05:04	10:12
2-Jicamarca (JICA)	−11.99	−76.0	−0.38	−2.21	05:02	10:06
3-Huancayo (LHYO)	−12.07	−75.21	−0.61	−2.75	04:54	09:54
4-Pucallpa (LPUC)	−8.39	−74.58	6.11	−4.05	04:52	09:50
5-São Luís (SALU)	−2.53	−44.31	−6.66	−19.43	04:53	07:50
6-Teresina (PITN)	−5.09	−42.80	−12.92	−19.97	04:46	07:37
7-Bacabal (MABB)	−4.22	−44.78	−9.19	−19.63	04:54	07:53
8-Belo Horizonte (MGBH)	−19.81	−43.95	−33.68	−20.56	04:45	07:40

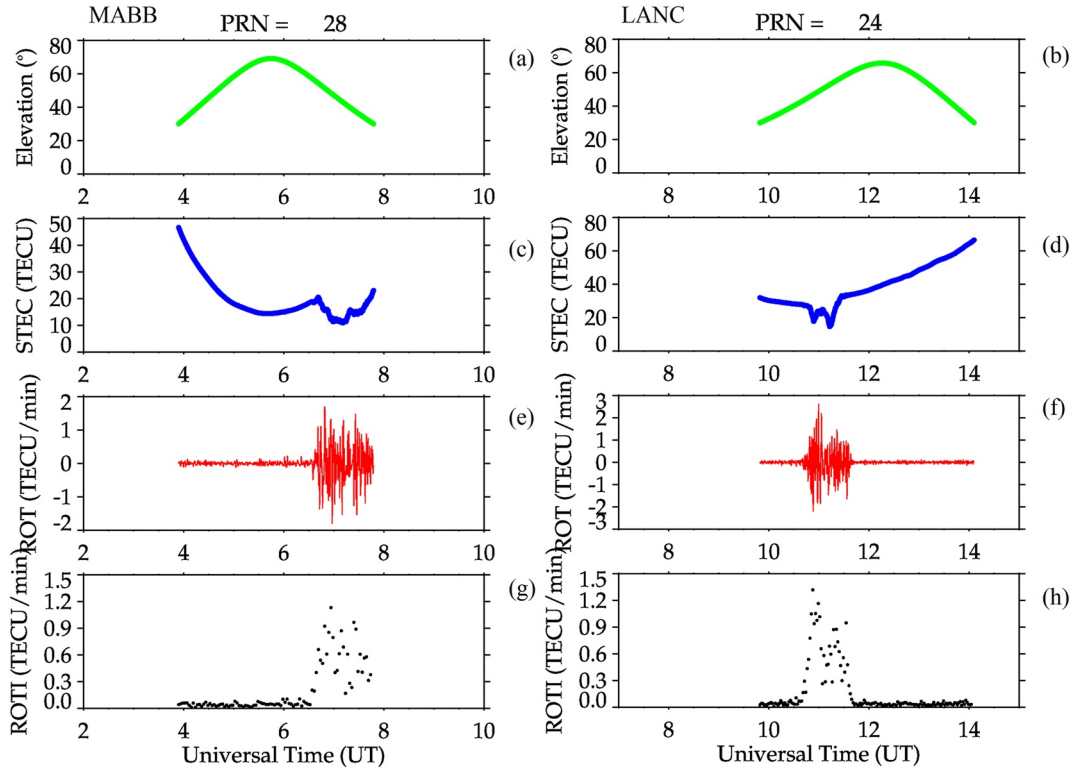

Figure 2. Elevation angle (a) and (b), relative slant total electron content (c) and (d), detrended Rate Of TEC (e) and (f), and Rate Of TEC Index (g) and (h) for MABB-PNR 28 and LANC-PRN 24 observations, respectively.

The ROTI was defined as the standard deviation of the detrended ROT given by Equation 3 (Pi et al., 2013), and the detrending helps remove the nominal geometric effect, subtracting the absolute values from the running average for all line-of-sight.

$$\mathrm{ROTI} = \sqrt{< \mathrm{ROT}^2 > - < \mathrm{ROT} >^2}, \tag{3}$$

where <> is the symbol of the arithmetic average, and the ROTI time resolution is 2.5 min interval.

In more detail, Figure 2 shows relative slant TEC, detrended ROT, and ROTI data obtained by processing data from station MABB (left) on the east coast for PRN 28 observations and from station LANC (right) on the west coast for PRN 24. The plotted data include elevation angle (a and b), relative STEC (c and d), detrended ROT (e and f), and ROTI (g and h), on 18 March 2015.

In Figure 2, the depletions in STEC (c and d) are evident from 06:30 UT to 08:00 UT in MABB station and from 10:30 UT to 11:30 UT in LANC station. The detrended ROT shows fluctuations at the same hours associated with these depletions, and ROTI increases simultaneously.

Additionally, with all the PRNs together an interpolation method is applied to produce ROTI and TEC maps to cover the whole South American continent. These TEC maps are generated from observation cells of 0.5° × 0.5° in latitude and longitude. The cell is built for 3 × 3 elements, corresponding to 1.5° × 1.5°. Then, if there is no Ionospheric Pierce Point (IPP) data in the area, the box is resized to 5 × 5 elements, corresponding to 2.5° × 2.5°, and so on. This method is applied up to 21 × 21 elements, corresponds to a maximum smooth of 10.5° × 10.5° (Carmo et al., 2021; Takahashi et al., 2016). The construction of ROTI maps follows the same procedure. The ionospheric shell height used in this work is set to 350 km.

2.2. Digisonde Data

Digisonde is a multifrequency radar operating in the high frequency (HF) band. The digisonde sends electromagnetic waves ranging from 1 to 30 MHz to the ionosphere that reflects the signal. As a result, the vertical profile of the ionospheric layers is measured and visualized in ionograms. In addition, some ionospheric parameters, such as the vertical electronic density ionospheric profile, the virtual height, the real height, and the ionospheric layer critical frequency, can be estimated using ionosondes (Reinisch et al., 2009).

In this paper, ionosondes at São Luís (SALU) and Jicamarca (JICA) were used to detect irregularities that are shown as Equatorial Spread F (ESF) echoes in ionograms, which are associated with EPB (Anderson & Mendillo, 1983). Locations of the ionosondes used in the study are shown in Figure 1b. ESF is detected in the ionosonde through signal scattering (Reinisch et al., 2009).

3. Results

The ionospheric response to the St. Patrick's Day magnetic storm (17–18 March 2015) has been analyzed in many studies (e.g., Astafyeva et al., 2015; Denardini et al., 2020; Fagundes et al., 2016; Figueiredo et al., 2017; Venkatesh et al., 2017). However, in-depth analyses of pre- and post-sunrise plasma bubbles generated during the St. Patrick's geomagnetic storm in the South American sector have not been reported in the literature. Thereby, our analysis is focused on revealing the main characteristics of the generation and duration of plasma bubbles around local dawn in this sector.

Figure 3 shows the Interplanetary Magnetic Field (IMF) Bz and By component (panel a, in purple and orange, respectively), the Auroral Electrojet (AE) index (panel b, in orange), the Dst index (panel c, in blue), and the ROTI measurements from all the GPS satellites in view for SALU and JICA (panels d and e, in blue, respectively; NB: ROTI is obtained at Ancon, which is very close to JICA) for 2 days of the storm. The $h'F$ curves and their quiet references (panels f and g, in red and black, respectively) for the same stations are shown. The $h'F$ quiet day (Qd) refers to 14 March 2015. Here $h'F$ denotes the virtual height of the ionosphere.

The Sudden Storm Commencement (SSC) was registered at 04:45 UT on 17 March 2015 (e.g., Astafyeva et al., 2015). Then, the IMF Bz turned southward at about 6:00 UT and remained this way for more than 18 hr with occasional northward turns (e.g., around 10:30 UT on March 17th). The lowest Dst value of −222 nT was recorded near 23:00 UT. There are other dynamical features in IMF, geomagnetic field, ionospheric F layer changes, etc., but here we focus on times when ionospheric irregularities and scintillation occurred around dawn at different longitudes in the South American sector.

Before 06:00 UT on March 18th, IMF Bz was weak though southward. F-layer at SALU increased after 3:00 UT compared with the quiet-time pattern, and ionospheric irregularities at the same site were observed in ROTI at about 07:00 UT (04:00 LT), which lasted until 11:30 UT (08:30 LT). During this period, a quick northward reversal of IMF Bz was recorded at 06:00 UT. At this time, the F-layer over JICA rose relatively to the Qd curve (01:00 LT). At nearby Ancon, the ROTI values increased between 10:00 UT and 13:00 UT (05:00 LT and 08:00 LT).

The upward plasma drift is observed with the elevation of the F-layer in the equatorial region in both longitudes. In the South America sector, the climatology of plasma drift is downward under quiet conditions (electric field is westward) before sunrise in March (Fejer, 2011). The observed F layer rise compared to the quiet time before the occurrence of irregularities during these hours (until 10:00 UT (07:00 LT) in SALU and 12:00 UT (07:00 LT) in JICA, see Figures 3f and 3g), appears to be an effect of the storm.

Statistics done by Scherliess and Fejer (1997) showed upward perturbations or turning of plasmas vertical drift during disturbed space weather periods in Jicamarca near dawn. This was attributed to the DDEF, which drives upward equatorial drifts with high amplitude near sunrise. This is consistent with the results presented here. Before dawn, our observations show that the F layer rises at 4 UT (∼1 LT) in SALU and at 6 UT (∼1 LT) in JICA, the same local time. The maximum layer elevation occurs at 7 UT (4 LT) in SALU and 11 UT (6 LT) in JICA when the EPBs started. Additionally, Fejer et al. (1999) observed irregularities at ∼4 LT when the vertical drifts of the disturbed dynamo showed greater amplitudes. This is also consistent with SALU observations.

We examine irregularities in these two longitude sectors on 18 March 2015. Three stations on the east coast and three stations on the west coast were selected for a more detailed analysis (see Figure 1a). Such analysis focuses

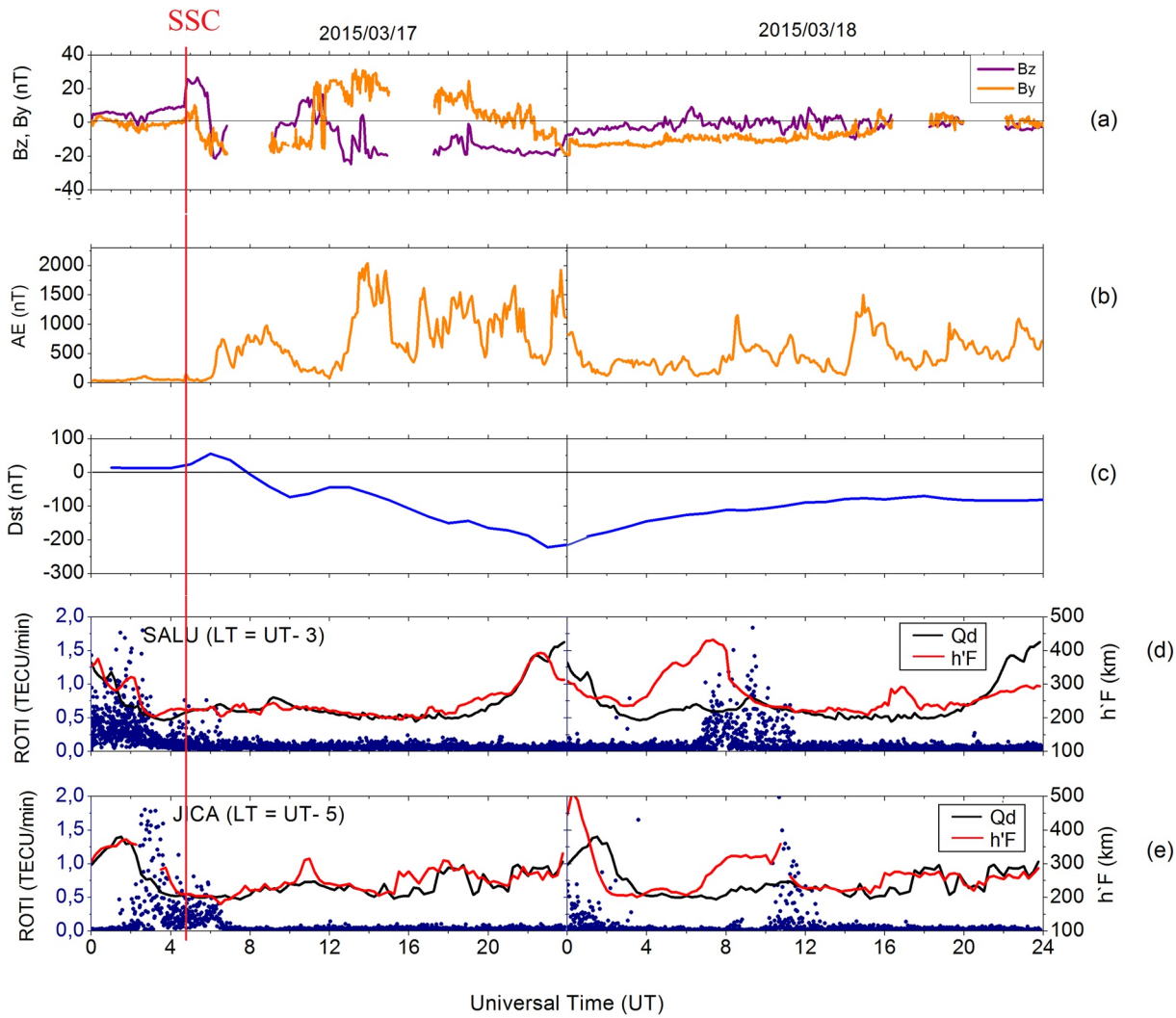

Figure 3. Interplanetary Magnetic Field *Bz* and *By* (panel a, in purple and orange, respectively), the Auroral Electrojet index (panel b, in orange), the Dst index (panel c, in blue) and Rate Of TEC Index for São Luís and Jicamarca/Ancon (panels d and e, in navy, respectively), along with the *h'F* curves and their quiet references (panels f and g, in red and black, respectively) for the same stations. The red line is the Sudden Storm Commencement, and the orange line is the sunrise.

on evaluating TEC and ROTI's temporal evolution. Figure 4 shows the ROTI measurements from all the GPS satellites in view (blue points) and TEC (orange curves) time variations for the selected sites in the east coast (SALU, panel a, MABB, panel b, and PITN, panel c) and the west coast (LANC, panel d, LHYO, panel e, and LPUC, panel f) stations.

Figure 4 shows ROTI measurements at six stations. The upper three panels show data from the east longitude sector, and the lower three panels show data in the west longitude sector. For each station, the ROTI measurements made from the single receiver to all satellites in view are over plotted together. An intensification of the ROTI occurred at the three east coast stations (panels a through c), starting at 6:30 UT on March 18 and lasted until approximately 11:30 UT at SALU and MABB, and until about 11:00 UT at PITN. The ROTI increases around 10:00 UT observed at the three stations on the west coast. In LANC, this increase lasted until 13:00 UT. On the other two stations (LHYO and LPUC) in the west, this increase lasted until 11:40 UT. According to Table 1, sunrise started at ~8 UT on the east coast and ~10 UT on the west coast. After sunrise, the irregularity persisted 3 and half hours on the east coast and ~2 hr on the west coast. As a result, the plasma irregularities lasted longer on the east coast (~5 hr) than on the west coast (~3 hr). Under normal conditions, the photoionization process generates plasma, and a decreased plasma density region can be filled by the newly created plasma

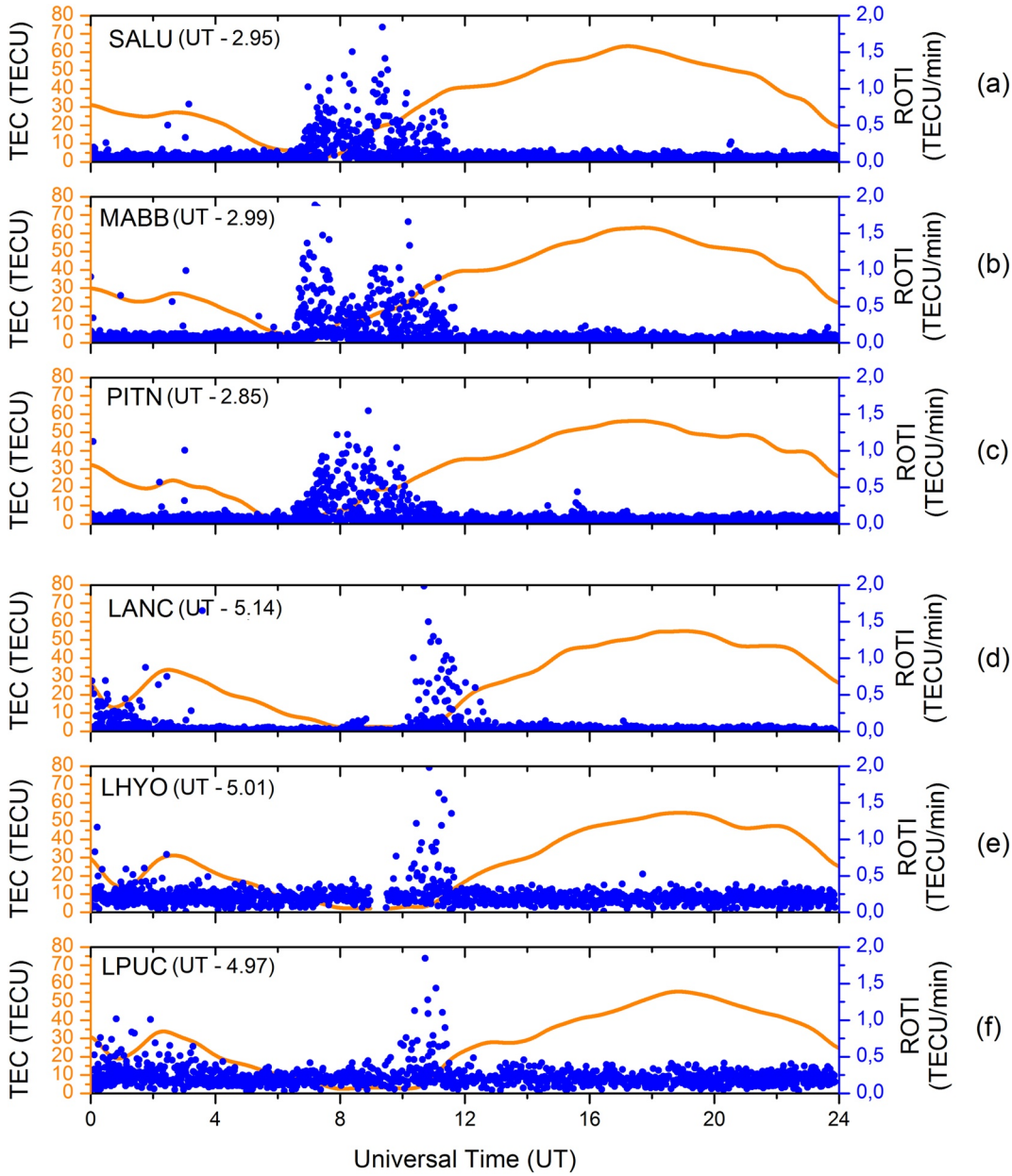

Figure 4. Temporal variations of vertical total electron content (TEC) (orange) above three stations (SALU, MABB, and PITN) in the east longitude sector and three stations (LANC, LHYO, and LPUC) in the west longitude sector on 18 March 2015, are shown in this figure. Along with TEC data, Rate Of TEC Index measurements (blue dots) made from the same single receiver to all satellites in view are also shown for the six stations.

during the process. Some previous study has suggested that the early morning recovery-phase of storms can contribute to long-lasting plasma depletions even with photoionization (Otsuka et al., 2021).

Figure 5 shows the maps of TEC (first column), ROTI (second column), and ionograms for SALU (third column) and JICA (fourth column) at 07:00, 08:00, 10:00, and 11:50 UT. The red line on maps is the magnetic equator, and the white dotted line is the solar terminator. A movie of ROTI map during these hours is provided in the Supporting Information S1 that readers can view.

In Figure 5, we can see the signature of pre-sunrise plasma depletions or bubbles on the TEC map (an example is identified with the red arrow). Additionally, these plasma bubbles are more evident on the ROTI map. Their field-aligned structure is more explicit, forming a reversed and rather flattened c-shape (e.g., Kil et al., 2009). At

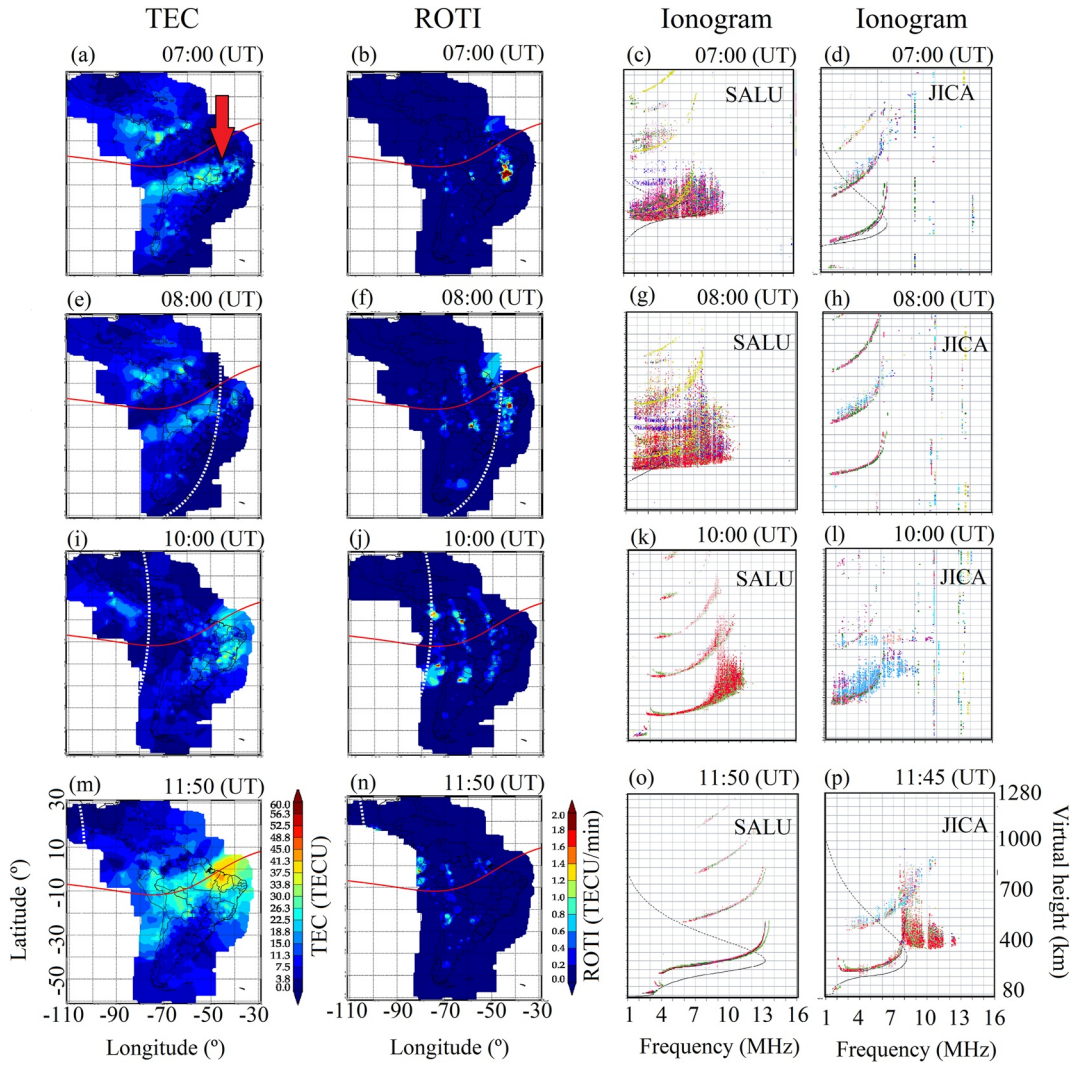

Figure 5. Total electron content maps (first column from the left), Rate Of TEC Index maps (second column), ionograms for São Luís (third column), and ionograms from Jicamarca (fourth column) at 07:00 UT, 08:00 UT, 10:00 UT, and 11:50 UT during 18 March 2015. The solid red line indicates the magnetic equator, and the dotted white line shows the solar terminator.

8:00 UT, the passage of the solar terminator at 300-km altitude occurs on the east coast. The solar terminator is almost completely off the map around 11:50 UT. Even then, we still see plasma bubble structures on the maps. The ionograms from SALU and JICA help confirm the time of occurrence of these plasma bubbles within the appearance of ESF at both stations.

4. Discussions

From the results by Kuai et al. (2016) on March 17th at 06:00 UT, an undershielding electric field was identified within the IMF *Bz* southward turning, in which the eastward prompt penetration electric field (PPEF) occurs on the dayside. At 10:00 UT, the presence of the westward equatorial electrojet was identified. In addition, a westward electric field perturbation of the overshielding effect was identified, with northward IMF *Bz*. The focus of this work is the evolution of the plasma bubbles generated in the recovery phase of this storm. Other perturbations during this storm have been studied by several authors (e.g., Astafyeva et al., 2015; Denardini et al., 2020; Kuai et al., 2016; Venkatesh et al., 2017; Verkhoglyadova et al., 2016; Zhang et al., 2017). Zakharenkova et al. (2019) observed these pre-dawn plasma bubbles and related their generation to DDEF. However, Huang et al. (2013) and Tulasi Ram et al. (2015) studied in regions other than Brazil, and Zakharenkova et al. (2019) did a global study.

These EPBs structures were so intense that even with sunrise and photoionization effects active were not enough for these structures to cease.

Here we discuss potential physical mechanisms responsible for the evolution and the dissipation of the plasma bubbles generated in the South American sector during the recovery phase of the St. Patrick's Day storm. We intend to emphasize three main points in this paper: possible DDEF effect, scintillation at or near minimum TEC, and longitudinal differences in scintillation and *E* layer.

4.1. Possible DDEF Effect

A prompt penetration of an undershielding electric field in eastward/westward direction on the day/night (Fejer et al., 2008) can be associated with turning of the IMF *Bz* to southward with an AE intensification. Also, the overshielding electric field can occur in the reversed direction when *Bz* turns northward (Fejer, 1991; Kelley et al., 1979). The disturbance dynamo effect is in the same direction as overshielding (Kikuchi, 2021), but the effect takes a longer time because the effects of energy input at high latitude, which results in Joule heating that affect thermosphere, take some time to reach equatorial latitudes (Blanc & Richmond, 1980; Fejer et al., 2008; Richmond & Roble, 1997). Figure 3 shows negative *Bz* with high values of AE at about 6 UT on March 17, as reported by Resende et al. (2021). Also, Huang et al. (2016) studied this storm and concluded that the DDEF started on March 17 at about ∼4 hr after SSC and lasted about 31 hr. Carter et al. (2016) reported that a possible overshielding electric field started at about 0 UT on March 18. After around 0 UT, the Bz starts to recovery. The rising of h'F compared with quiet days at about 3 UT on SALU and before 7UT on JICA seems to be associated with the eastward electric field due to DDEF (e.g., Fejer et al., 1983), which can set the preconditions for RTI. There is also an AE increase after 8 UT while IMF *Bz* and *By* do not show apparent changes. It appears that the AE increase may be caused by substorms, which may play a role in affecting conditions in Jicamarca where EPBs occurred about 2 hours later.

One of the major dynamical effects during a geomagnetic storm is disturbance dynamo that generates electric field perturbations at low latitudes, due to neutral wind perturbations caused by the joule heating (Blanc & Richmond, 1980; Fejer & Scherliess, 1997; Fejer et al., 1983; Mazaudier & Venkateswaran, 1990; Wolf, 1995). It could occur in the nighttime sectors during storms and show longitudinal distribution effects (Huang, 2013; Huang et al., 2005; Maruyama et al., 2005). In the ionosonde data (Figure 3) we identify *F* layer rising from ∼3:00 to 9:00 UT at SALU and from ∼7:00 to 12:00 UT at JICA. We see IMF *Bz* near zero during the plasma bubbles hours, but the AE increase indicates increased activity in the polar region that may have effect added to the pre-existing effects of the magnetic storm (e.g., Fejer, 1997; Fejer & Scherliess, 1997; Scherliess & Fejer, 1997). We then turn to look at the wind data taken using the FPI, which is plotted in Figure 6.

Figure 6 shows the neutral wind component, zonal in red and meridional in blue compared with the average of quiet days in gray. In the JICA FPI data we observe significant disturbances in the wind component. Unfortunately wind data in SALU longitude is not available, and no comparison can be made between wind in the two longitudes though we also see the *F* layer rise in the ionosonde data in the east coast. Nevertheless the wind perturbation measured by FPI between ∼8 and 10 UT at JICA appears coincident with the h'F rising, in the same hours, and the wind perturbation shows greater amplitudes at about 4 LT (e.g., Fejer, 2002; Fejer et al., 1999). Northward meridional wind generates a positive gradient in latitude that stabilizes the influence of the Rayleigh-Taylor instability (Huba & Krall, 2013), then increasing the F-layer peak (Fejer, 1993). The disturbed wind and the *F* layer rise brings up a possibility of DDEF effects at the equator in the Jicamarca longitude, due to global circulation caused by energy input into the auroral region creating currents and causing the disturbed wind directed toward the equator and low latitudes (Blanc & Richmond, 1980). Then, plasma irregularities following the wind perturbation and *F* layer rising seem to indicate a possibility of DDEF effects at the equator in the Jicamarca longitude at the time.

Huang (2013) reported that in magnetic storms during equinoxes, at midnight, the zonal component of DDEF can be eastward at midnight or post-midnight sectors. Compared with the climatological pattern and IMF *Bz* as well as magnetospheric *Ey* observations (Figure 3), the disturbance wind dynamo seems to be a reasonable mechanism that can cause eastward zonal electric field enhancement and rise of the *F* layer. The storm-time dynamical effect can then help trigger the RTI at low latitudes and cause EPBs and irregularities.

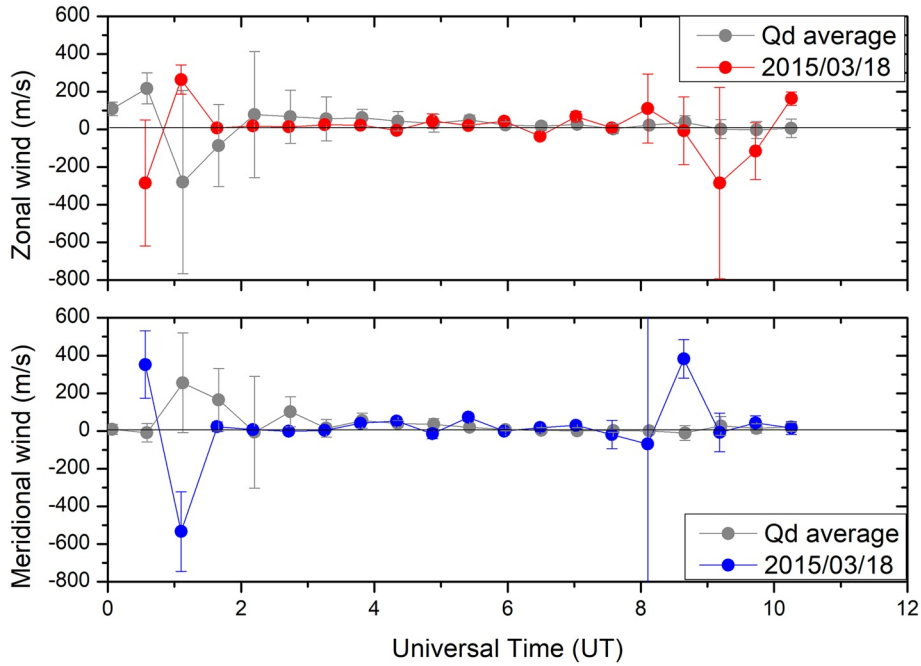

Figure 6. The zonal (red) and meridional (red) wind in Jicamarca derived from the FPI measurements, with the corresponding error bar, and the average of four quiet days (gray) in March according to GFZ-Potsdam (https://www.gfz-potsdam.de/en/kp-index/) that is 10, 30, 5, and 14 March 2015.

Hui and Vichare (2021) studied the effects of IMF *By* on the evening and morning pre-reversal enhancement (PRE) in the equatorial zonal electric field using TIE-GCM (e.g., Heelis et al., 1982; Weimer, 2005). They suggested that morning PRE may not be related to IMF *By* but may be related to the effects of a disturbed dynamo. Their modeling study also shows that IMF *By*'s positive and negative conditions are oppositely related to the perturbations of meridional winds at the equator. Moreover, they suggested that this opposition is responsible for the effects observed in the morning and post-sunset PRE as DDEF is present. Our observations show wind perturbations at dawn when IMF *By* is negative, which seems to agree with Hui and Vichare's (2021) study (Figure 3a). In addition, we also ran TIE-GCM to investigate the behavior of the vertical drift velocity, as shown in Figure 7. Our TIE-GCM model run take inputs of F10.7 cm solar radio flux and K_p index. The model output is examined at UT and locations (latitude, longitude, and altitude) of interest.

Figure 7 shows disturbances in the plasma vertical drift velocity starting before 5 UT (upward) in JICA and in SALU, which coincide with the h'F elevation times, shown in Figures 3d and 3e. TIEGCM is a self-consistent coupled thermospheric-ionospheric model, and for this model run its electric field perturbations are driven by

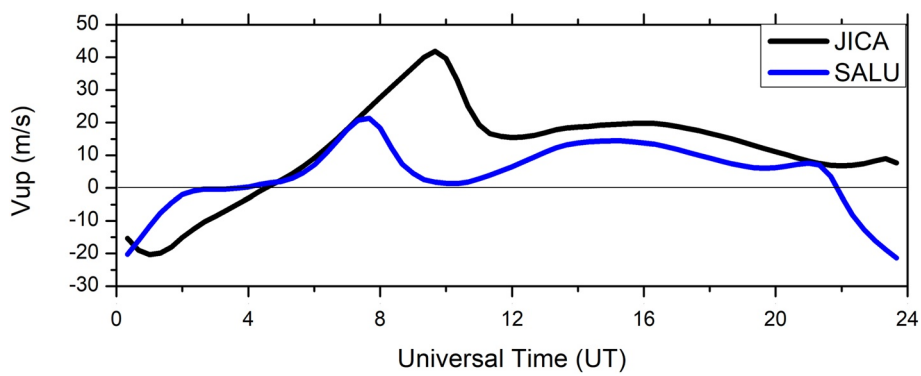

Figure 7. Plasma vertical drift velocity (V_{up}) versus UT in Jicamarca (black) and São Luís (blue), given by TIE-GCM model, on 18 March 2015.

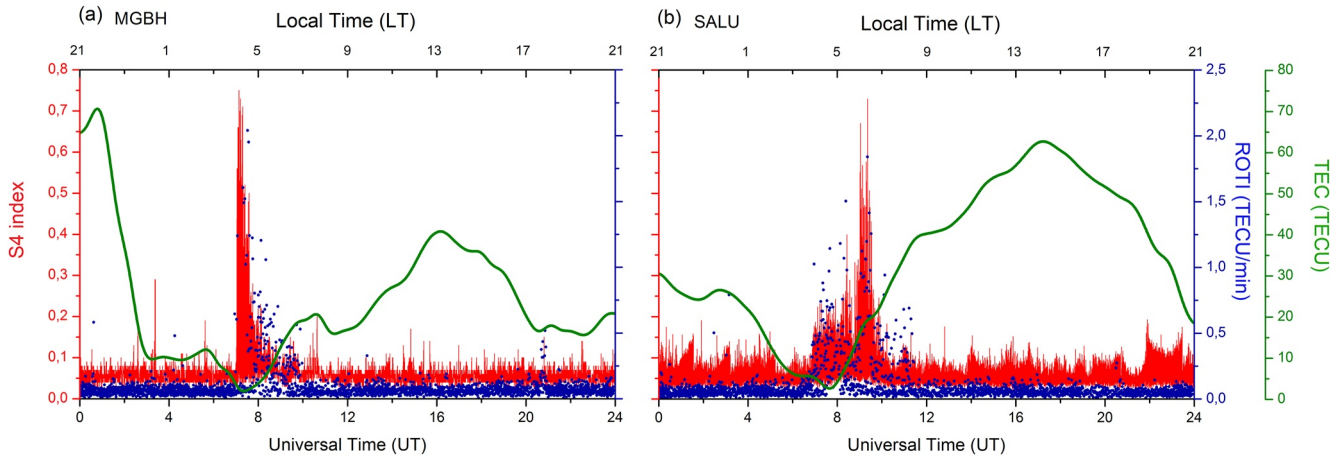

Figure 8. S4 index (red) and Rate Of TEC Index (blue dots) measurements from multiple Global Positioning System (GPS) satellites are overplotted versus UT for the MGBH (panel a) and SALU (panel b) stations, respectively, along with total electron content (green) above the two stations derived from the GPS data.

wind perturbation dynamo without the penetration mechanism or input. It appears that the electric field perturbations of the TIEGCM modeling support the DDEF hypothesis, because in this model run TIEGCM does not include electric field penetration so that electric field perturbation is considered as a DDEF effect. Previously, Fejer et al. (2017) noted that the observational data are similar to the TIEGCM model in Jicamarca. The equatorial vertical drifts due to the disturbance dynamo presented by Fejer and Richmond show a similar perturbation pattern through the TIEGCM run. Furthermore, the modeled plasma drift velocity perturbations are consistent with ionosonde observations.

Su et al. (2009) suggested that the cause of the dawn scintillation is similar to that of the sunset, but they didn't explain why the irregularities last long hours after sunrise. In the case study here, we suggest that the disturbed dynamo electric fields at sunrise caused the rise of the layer. We also considered PPEF and possible overshielding effect, but the corresponding Bz southward turning followed by northward turning cannot be identified in IMF Bz data. Hence there is no apparent evidence to suggest PPEF and overshilding effects in this case.

4.2. Scintillation at Minimum TEC

Occurrences of ionospheric scintillations were observed using GNSS scintillation receivers that provide S4 index measurements. S4, ROTI and TEC measurements are shown together for the MGBH and SALU stations in a similar longitude (Table 1) in Figure 8.

Figure 8a shows strong amplitude scintillation indicated by the S4 index, and intense ROTI are observed at the MGBH station at dawn and at the SALU station after sunrise. We notice that sunrise time was about 04:45 LT in MGBH and 04:53 LT in SALU (see Table 1), respectively.

Strong scintillation at dawn and post-sunrise when ionospheric electron density and TEC were minimum (according to observations at MGBH station) and near the minimum (at SALU station) is not common. Our observations show that strong L-band scintillation can occur when the ambient TEC reaches minimum values, which makes numerical simulation of diurnal plasma bubbles in existing models difficult (e.g., Kil et al., 2015; Yokoyama et al., 2015). Our observations suggest that related modeling needs to address strong amplitude scintillation under a low or minimum TEC environment.

4.3. Longitudinal Dependence and Its Differences in Scintillation and *E* Layer

We compare observations on the east and west coasts. As shown in Figure 4 and Table 1, on the east coast, the irregularities associated with plasma bubbles lasted on average 3.5 hr after sunrise (1.5 hr before sunrise) in SALU and MABB, and PITN. The irregularities on the west coast did not last long after sunrise. These observations show a distinguished longitudinal dependence: the post-sunrise durations of plasma bubbles are different between the two longitude sectors.

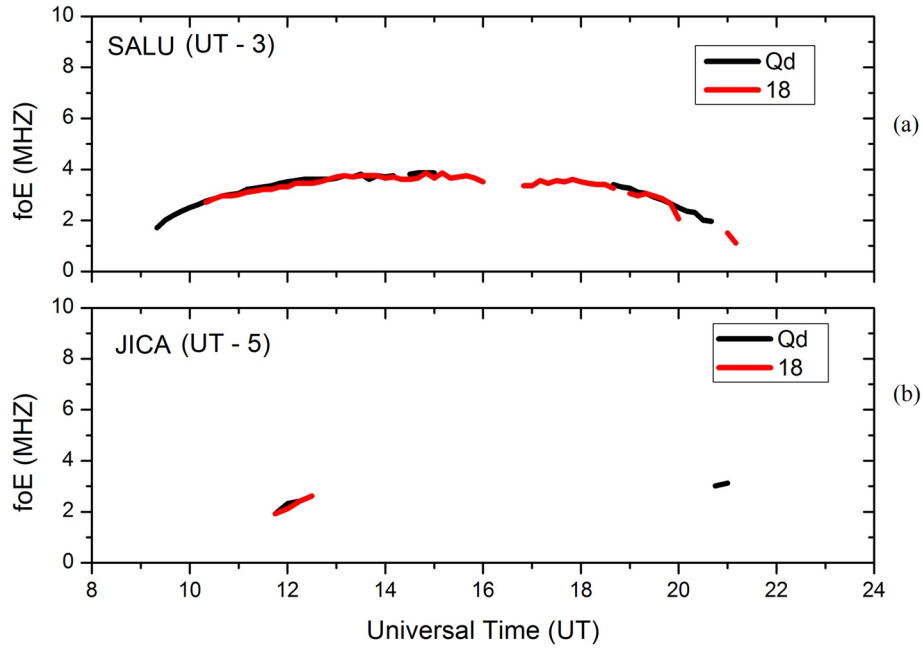

Figure 9. Critical frequency of region *E* (*foE*) in São Luís (panel a), and JICA (panel b), on 18 March 2015 (red), compared to the calm day (Qd). The data gap in the plot means the *E* layer is not detectable.

The upward drift of the equatorial *F* layer ($E \times B$) generates favorable conditions for the RTI development (Aarons, 1991; Fejer et al., 1999). The dissipation of these plasma irregularities occurs when the *E* layer appears. This is caused by the high density and conductivity of this region, as a consequence the electric fields would be short-circuited by the Pedersen conductivity, reducing the linear growth rate of the EPBs (Chou et al., 2020).

Burke (1979) investigated the disappearance of EPBs after sunrise using modeling. He explains that after sunrise, the conducting *E* region could discharge the electric field inside the plasma bubbles and prevent the growth of these irregularities. Zalesak et al. (1982) performed a numerical simulation and concluded that even without accounting for thermospheric neutral wind, the *E* region would be capable of extinguishing the plasma bubbles due to the above mechanism.

To investigate if the *E* region has an impact on the duration of these EPBs in the east coast and west coast longitudes, we obtained the critical frequency of the *E* region (*foE*) in SALU (panel a) and JICA (panel b), shown in Figure 9.

Although the JICA *foE* data during the majority of hours of interest are not useable (Figure 9b), due to the presence of the sporadic Es layer (Taieb et al., 1975), the readable data show that the *E* layer appeared after about 11:30 UT. On the other hand, the *E* layer at SALU (panel a) appeared after ~10:30 UT, about 1 hour later than the Qd day. It is interesting to note that the *E* layer appears on the east coast later than that during the Qd, which may make the EPBs stay longer after sunrise in this region. Also, the data gap in the plot means the *E* layer is not detectable by the ionosonde at the time. The differences of *E* region occurrence and the duration of post-sunrise irregularities between the east coast and west coast appear to support the idea that the EPBs dissipated after the emergence of the *E* region, which occurred in the west coast sector, while the delay of the *E* region and the longer duration of irregularities in the east coast sector seem to be consistent with this idea.

In addition, besides the 33° longitude difference (3,600 km) and a different impact of the E-region effect between these two sets of GNSS stations (on the east and west coasts), there is also a significant difference in the declination of the magnetic equator between these two longitude sectors, being ~−2° on the west coast while ~−20° on the east coast, as shown in Table 1.

Abdu et al. (1992) demonstrated that magnetic declination could control the development of EPBs. They showed that the efficiency of growth of plasma irregularity could decrease when there is an almost perfect alignment

of the terminator with the magnetic meridian, and small angles contribute to the plasma irregularities development. In addition, the F region dynamo generation is also affected by the magnetic field's declination (Abdu et al., 1981). Nevertheless, their studies suggest that magnetic declination may contribute to the differences found in the evolution of the EPBs observed in the east and west coasts, such as their emergence, duration, and dissipation, which may contribute to longitudinal difference between the duration of EPBs after sunrise in the two longitudes.

5. Conclusions

Plasma bubbles over South America were detected around dawn (before and after sunrise) by using two-dimensional TEC and ROTI maps and ionosonde measurements during the recovery phase of the 2015 St. Patrick's Day storm on March 18. The plasma bubbles observed on the east coast of Brazil remained approximately 3 and half hours during the daytime after sunrise. Characteristics, duration, and generation of EPBs, and ionospheric irregularities were studied using GNSS, ionosonde, and FPI observations. The observed major features are summarized below:

1. The generation of these dawn and post-dawn plasma bubbles appears to be triggered under a possible effect of wind disturbance dynamo in the recovery phase of the magnetic storm, when wind perturbations and equatorial *F* layer rising occur coincidently followed by the occurrence of plasma bubbles.
2. The ionospheric plasma bubbles and associated irregularities remained 3.5 hr during the daytime after sunrise on the east coast of Brazil.
3. Analysis of observations suggests a longitudinal dependency in the duration of post-sunrise scintillation within 33° in longitude difference (~3,000 km).
4. Strong ionospheric scintillation is observed when TEC is minimum and after sunrise in the context of ionospheric diurnal variation.
5. After sunrise, the duration of plasma bubbles seems to be consistent with the delay in the emergence of the *E* layer.

Data Availability Statement

Website required login—South America receivers Rinex files are available on the Embrace/INPE Space Weather Program website (http://www2.inpe.br/climaespacial/SWMonitorUser/faces/adm/tec/downloadFiles.xhtml). The Website required login—Peru receivers Rinex (http://lisn.igp.gob.pe/jdata/database/). Complementary Rinex data (UNAVCO, https://www.unavco.org/data/gps-gnss/gps-gnss.html). The Website required login—Orbit data website (https://urs.earthdata.nasa.gov/home). The Website required login—Wind data from Fabry-Perot Interferometer (http://cedar.openmadrigal.org/single). Ionosonde data (https://lgdc.uml.edu/common/DIDB-FastStationList). The parameters *By*, *Bz*, *AE* (https://omniweb.gsfc.nasa.gov/form/omni_min.html). The Dst index (http://wdc.kugi.kyoto-u.ac.jp/dst_provisional/201503/index.html). The Website required login—S4 index (https://ismrquerytool.fct.unesp.br/is/ismrtool/retrieval/download_ismr.php). The declination and dip angle for each station (http://geomag.bgs.ac.uk/data_service/models_compass/igrf_calc.html). Sunrise information (https://www.timeanddate.com/sun/). HWM-14 on the support information by Drob et al. (2015), and Software TEC (https://seemala.blogspot.com/). TIE-GCM model (https://ccmc.gsfc.nasa.gov/requests/IT/TIE-GCM/tiegcm_user_registration.php).

Acknowledgments
C. S. Carmo thanks CNPq/MCTIC (Grant 141935/2020-0 and 150261/2022-5). C. M. Denardini thanks CNPq/MCTIC (Grant 303643/2017-0). C. A. O. B., Figueiredo thanks FAPESP (Grant 2018/09066-8 and 2019/22548-4). G. A. S. Picanço thanks CAPES/MEC (Grant 88887.351778/2019-00). A portion of the work was carried out at the Jet Propulsion Laboratory, California Institute of Technology, under a contract with NASA. We thank the Community Coordinated Modeling Center (CCMC) for providing the Thermosphere-Ionosphere- Electrodynamics General Circulation Model (TIE-GCM) results. We thank the Brazilian Space Agency and the Brazilian Ministry of Science, Technology and Innovation.

References

Aarons, J. (1991). The role of the ring current in the generation or inhibition of equatorial F layer irregularities during magnetic storms. *Radio Science*, *26*(4), 1131–1149. https://doi.org/10.1029/91RS00473

Abdu, M., Batista, I., Reinisch, B., MacDougall, J., Kherani, E., & Sobral, J. (2012). Equatorial range spread F echoes from coherent backscatter, and irregularity growth processes, from conjugate point digital ionograms. *Radio Science*, *47*(6), 1–8. https://doi.org/10.1029/2012RS005002

Abdu, M., Batista, I., Takahashi, H., MacDougall, J., Sobral, J., Medeiros, A., & Trivedi, N. (2003). Magnetospheric disturbance induced equatorial plasma bubble development and dynamics: A case study in Brazilian sector. *Journal of Geophysical Research: Space Physics*, *108*(A12), 1449. https://doi.org/10.1029/2002JA009721

Abdu, M. A. (2012). Equatorial spread F/plasma bubble irregularities under storm time disturbance electric fields. *Journal of Atmospheric and Solar-Terrestrial Physics*, *75*, 44–56. https://doi.org/10.1016/j.jastp.2011.04.024

Abdu, M. A., Alam Kherani, E., Batista, I. S., de Paula, E. R., Fritts, D. C., & Sobral, J. H. A. (2009). Gravity wave initiation of equatorial spread F/plasma bubble irregularities based on observational data from the SpreadFEx campaign. *Annales Geophysicae*, *27*(7), 2607–2622. https://doi.org/10.5194/angeo-27-2607-2009

Abdu, M. A., Batista, I. S., & Sobral, J. H. A. (1992). A new aspect of magnetic declination control of equatorial spread F and F region dynamo. *Journal of Geophysical Research*, *97*(A10), 14897–14904. https://doi.org/10.1029/92JA00826

Abdu, M. A., Bittencourt, J. A., & Batista, I. S. (1981). Magnetic declination control of the equatorial F region dynamo electric field development and spread F. *Journal of Geophysical Research*, *86*(A13), 11443–11446. https://doi.org/10.1029/JA086iA13p11443

Agyei-Yeboah, E., Fagundes, P. R., Tardelli, A., Pillat, V. G., Pignalberi, A., Kavutarapu, V., et al. (2021). Ground and satellite-based observations of ionospheric plasma bubbles and blobs at 5.65° latitude in the Brazilian sector. *Advances in Space Research*, *67*(8), 2416–2438. https://doi.org/10.1016/j.asr.2021.01.034

Anderson, D. N., & Mendillo, M. (1983). Ionospheric conditions affecting the evolution of equatorial plasma depletions. *Geophysical Research Letters*, *10*(7), 541–545. https://doi.org/10.1029/gl010i007p00541

Arruda, D. C., Sobral, J. H. A., Abdu, M. A., Castilho, V. M., Takahashi, H., Medeiros, A. F., & Buriti, R. A. (2006). Theoretical and experimental zonal drift velocities of the ionospheric plasma bubbles over the Brazilian region. *Advances in Space Research*, *38*(11), 2610–2614. https://doi.org/10.1016/j.asr.2006.05.015

Astafyeva, E., Zakharenkova, I., & Förster, M. (2015). Ionospheric response to the 2015 St. Patrick's Day storm: A global multi-instrumental overview. *Journal of Geophysical Research: Space Physics*, *120*(10), 9023–9037. https://doi.org/10.1002/2015JA021629

Barros, D., Takahashi, H., Wrasse, C. M., & Figueiredo, C. A. O. (2018). Characteristics of equatorial plasma bubbles observed by TEC map based on ground-based GNSS receivers over South America. *Annales Geophysicae*, *36*(1), 91–100. https://doi.org/10.5194/angeo-36-91-2018

Blanc, M., & Richmond, A. D. (1980). The ionospheric disturbance dynamo. *Journal of Geophysical Research*, *85*(A4), 1669–1686. https://doi.org/10.1029/JA085iA04p01669

Burke, W. I. (1979). Plasma bubbles near the dawn terminator in the topside ionosphere. *Planetary and Space Science*, *27*(9), 1187–1193. https://doi.org/10.1016/0032-0633(79)90138-7

Carmo, C. S., Denardini, C. M., Figueiredo, C. A. O. B., Resende, L. C. A., Picanço, G. A. S., Neto, P. F. B., et al. (2021). Evaluation of different methods for calculating the ROTI index over the Brazilian sector. *Radio Science*, *56*(8), e2020RS007140. https://doi.org/10.1029/2020RS007140

Carter, B. A., Yizengaw, E., Pradipta, R., Retterer, J. M., Groves, K., Valladares, C., et al. (2016). Global equatorial plasma bubble occurrence during the 2015 St. Patrick's Day storm. *Journal of Geophysical Research - A: Space Physics*, *121*, 894– 905. https://doi.org/10.1002/2015JA022194

Cherniak, I., Krankowski, A., & Zakharenkova, I. (2018). ROTI maps: A new IGS ionospheric product characterizing the ionospheric irregularities occurrence. *GPS Solutions*, *22*(3), 69. https://doi.org/10.1007/s10291-018-0730-1

Chou, M.-Y., Wu, Q., Pedatella, N. M., Cherniak, I., Schreiner, W. S., & Braun, J. (2020). Climatology of the equatorial plasma bubbles captured by FORMOSAT-3/COSMIC. Journal of. *Geophysical Research: Space Physics*, *125*(5), e2019JA027680. https://doi.org/10.1029/2019JA027680

de Jesus, R., Batista, I. S., Takahashi, H., de Paula, E. R., Barros, D., Figueiredo, C. A. O. B., et al. (2020). Morphological features of ionospheric scintillations during high solar activity using GPS observations over the South American sector. *Journal of Geophysical Research: Space Physics*, *125*(3), JA027441. https://doi.org/10.1029/2019JA027441

Denardini, C. M., Picanço, G. A. S., Barbosa Neto, P. F., Nogueira, P. A. B., Carmo, C. S., Resende, L. C. A., et al. (2020). Ionospheric scale index map based on TEC data during the Saint Patrick magnetic storm and EPBs. *Space Weather*, *18*, e2019SW002330. https://doi.org/10.1029/2019SW002330

De Paula, E. R., Kherani, E. A., Abdu, M. A., Batista, I. S., Sobral, J. H. A., Kantor, I. J., et al. (2007). Characteristics of the ionospheric F-region plasma irregularities over Brazilian longitudinal sector. 94.20. Yx; 94.20. Vv; 94.20. Retrieved from http://nopr.niscair.res.in/handle/123456789/4706

De Rezende, L. F. C., De Paula, E. R., Kantor, I. J., & Kintner, P. M. (2007). Mapping and survey of plasma bubbles over Brazilian territory. *Journal of Navigation*, *60*(1), 69–81. https://doi.org/10.1017/S0373463307004006

Drob, D. P., Emmert, J. T., Meriwether, J. W., Makela, J. J., Doornbos, E., Conde, M., et al. (2015). An update to the Horizontal Wind Model (HWM): The quiet time thermosphere. *Earth and Space Science*, *2*(7), 301–319. https://doi.org/10.1002/2014EA000089

Fagundes, P. R., Cardoso, F. A., Fejer, B. G., Venkatesh, K., Ribeiro, B. A. G., & Pillat, V. G. (2016). Positive and negative GPS-TEC ionospheric storm effects during the extreme space weather event of March 2015 over the Brazilian sector. *Journal of Geophysical Research: Space Physics*, *121*(6), 5613–5625. https://doi.org/10.1002/2015JA022214

Fejer, B. G. (1991). Low latitude electrodynamic plasma drifts: A review. *Journal of Atmospheric and Terrestrial Physics*, *53*(8), 677–693. https://doi.org/10.1016/0021-9169(91)90121-M

Fejer, B. G. (1993). F region plasma drifts over Arecibo: Solar cycle, seasonal, and magnetic activity effects. *Journal of Geophysical Research*, *98*(A8), 13645–13652. https://doi.org/10.1029/93JA00953

Fejer, B. G. (1997). The electrodynamics of the low-latitude ionosphere: Recent results and future challenges. *Journal of Atmospheric and Solar-Terrestrial Physics*, *59*(13), 1465–1482. https://doi.org/10.1016/S1364-6826(96)00149-6

Fejer, B. G. (2002). Low latitude storm time ionospheric electrodynamics. *Journal of Atmospheric and Solar-Terrestrial Physics*, *64*(12–14), 1401–1408. https://doi.org/10.1016/S1364-6826(02)00103-7

Fejer, B. G. (2011). Low latitude ionospheric electrodynamics. *Space Science Reviews*, *158*(1), 145–166. https://doi.org/10.1007/s11214-010-9690-7

Fejer, B. G., Blanc, M., & Richmond, A. D. (2017). Post-storm middle and low-latitude ionospheric electric fields effects. *Space Science Reviews*, *206*(1–4), 407–429. https://doi.org/10.1007/s11214-016-0320-x

Fejer, B. G., Jensen, J. W., & Su, S.-Y. (2008). Seasonal and longitudinal dependence of equatorial disturbance vertical plasma drifts. *Geophysical Research Letters*, *35*(20), L20106. https://doi.org/10.1029/2008GL035584

Fejer, B. G., Larsen, M. F., & Farley, D. T. (1983). Equatorial disturbance dynamo electric fields. *Geophysical Research Letters*, *10*(7), 537–540. https://doi.org/10.1029/GL010i007p00537

Fejer, B. G., & Scherliess, L. (1997). Empirical models of storm time equatorial zonal electric fields. *Journal of Geophysical Research*, *102*(A11), 24047–24056. https://doi.org/10.1029/97JA02164

Fejer, B. G., Scherliess, L., & de Paula, E. R. (1999). Effects of the vertical plasma drift velocity on the generation and evolution of equatorial spread F. *Journal of Geophysical Research*, *104*(A9), 19859–19869. https://doi.org/10.1029/1999JA900271

Figueiredo, C. A. O. B., Wrasse, C. M., Takahashi, H., Otsuka, Y., Shiokawa, K., & Barros, D. (2017). Large-scale traveling ionospheric disturbances observed by GPS dTEC maps over North and South America on Saint Patrick's Day storm in 2015. *Journal of Geophysical Research: Space Physics*, *122*(4), 4755–4763. https://doi.org/10.1002/2016JA023417

Heelis, R. A., Lowell, J. K., & Spiro, R. W. (1982). A model of the high-latitude ionospheric convection pattern. *Journal of Geophysical Research*, *87*(A8), 6339–6345. https://doi.org/10.1029/JA087iA08p06339

Huang, C. M. (2013). Disturbance dynamo electric fields in response to geomagnetic storms occurring at different universal times. *Journal of Geophysical Research: Space Physics*, *118*(1), 496–501. https://doi.org/10.1029/2012JA018118

Huang, C.-M., Richmond, A. D., & Chen, M.-Q. (2005). Theoretical effects of geomagnetic activity on low-latitude ionospheric electric fields. *Journal of Geophysical Research*, *110*(A5), A05312. https://doi.org/10.1029/2004JA010994

Huang, C. S., de La Beaujardiere, O., Roddy, P. A., Hunton, D. E., Ballenthin, J. O., & Hairston, M. R. (2013). Long-lasting daytime equatorial plasma bubbles observed by the C/NOFS satellite. *Journal of Geophysical Research: Space Physics*, *118*(5), 2398–2408. https://doi.org/10.1002/jgra.50252

Huang, C.-S., Wilson, G. R., Hairston, M. R., Zhang, Y., Wang, W., & Liu, J. (2016). Equatorial ionospheric plasma drifts and O+ concentration enhancements associated with disturbance dynamo during the 2015 St. Patrick's Day magnetic storm. *Journal of Geophysical Research: Space Physics*, *121*(8), 7961–7973. https://doi.org/10.1002/2016JA023072

Huba, J. D., & Krall, J. (2013). Impact of meridional winds on equatorial spread F: Revisited. *Geophysical Research Letters*, *40*(7), 1268–1272. https://doi.org/10.1002/grl.50292

Hui, D., & Vichare, G. (2021). Influence of IMF-by on the equatorial ionospheric plasma drifts: TIEGCM simulations. *Journal of Geophysical Research: Space Physics*, *126*(9), e2021JA029270. https://doi.org/10.1029/2021JA029270

Kelley, M. C. (2009). *The Earth's ionosphere: Plasma physics and electrodynamics*. Academic press.

Kelley, M. C., Fejer, B. G., & Gonzales, C. A. (1979). An explanation for anomalous equatorial ionospheric electric fields associated with a northward turning of the interplanetary magnetic field. *Geophysical Research Letters*, *6*(4), 301–304. https://doi.org/10.1029/GL006i004p00301

Kikuchi, T. (2021). Penetration of the magnetospheric electric fields to the low latitude ionosphere. In C. Huang, G. Lu, Y. Zhang, & L. J. Paxton (Eds.), *Ionosphere dynamics and applications*. https://doi.org/10.1002/9781119815617.ch14

Kil, H., Heelis, R. A., Paxton, L. J., & Oh, S.-J. (2009). Formation of a plasma depletion shell in the equatorial ionosphere. *Journal of Geophysical Research*, *114*(A11), A11302. https://doi.org/10.1029/2009JA014369

Kil, H., Kwak, Y.-S., Lee, W. K., Krall, J., Huba, J. D., & Oh, S.-J. (2015). Nonmigrating tidal signature in the distributions of equatorial plasma bubbles and prereversal enhancement. J. *Geophys. Res. Space Physics*, *120*(4), 3254–3262. https://doi.org/10.1002/2014JA020908

Kuai, J., Liu, L., Liu, J., Sripathi, S., Zhao, B., Chen, Y., et al. (2016). Effects of disturbed electric fields in the low-latitude and equatorial ionosphere during the 2015 St. Patrick's Day storm. *Journal of Geophysical Research: Space Physics*, *121*(9), 9111–9126. https://doi.org/10.1002/2016JA022832

Magdaleno, S., Herraiz, M., & de La Morena, B. A. (2012). Characterization of equatorial plasma depletions detected from derived GPS data in South America. *Journal of Atmospheric and Solar-Terrestrial Physics*, *74*, 136–144. https://doi.org/10.1029/2020JA028544

Maruyama, N., Richmond, A. D., Fuller-Rowell, T. J., Codrescu, M. V., Sazykin, S., Toffoletto, F. R., et al. (2005). Interaction between direct penetration and disturbance dynamo electric fields in the storm-time equatorial ionosphere. *Geophysical Research Letters*, *32*, L17105. https://doi.org/10.1029/2005GL023763

Mazaudier, C., & Venkateswaran, S. V. (1990). Delayed ionospheric effects of March 22, 1979 studied by the sixth co-ordinated data analysis workshop (CDAW-6). *Annales Geophysicae*, *8*, 511–518.

Mrak, S., Semeter, J., Nishimura, Y., & Coster, A. J. (2021). Extreme low-latitude total electron content enhancement and Global Positioning System scintillation at dawn. *Space Weather*, *19*(9), e2021SW002740. https://doi.org/10.1029/2021SW002740

Otsuka, Y. (2018). Review of the generation mechanisms of post-midnight irregularities in the equatorial and low-latitude ionosphere. *Progress in Earth and Planetary Science*, *5*(1), 1–13. https://doi.org/10.1186/s40645-018-0212-7

Otsuka, Y., Shinbori, A., Sori, T., Tsugawa, T., Nishioka, M., & Huba, J. D. (2021). Plasma depletions lasting into daytime during the recovery phase of a geomagnetic storm in May 2017: Analysis and simulation of GPS total electron content observations. *Earth and Planetary Physics*, *5*(5), 427–434. https://doi.org/10.26464/epp2021046

Pi, X., Mannucci, A. J., Lindqwister, U. J., & Ho, C. M. (1997). Monitoring of global ionospheric irregularities using the Worldwide GPS Network. *Geophysical Research Letters*, *24*(18), 2283–2286. https://doi.org/10.1029/97GL02273

Pi, X., Mannucci, A. J., Valant-Spaight, B., Bar-Sever, Y., Romans, L. J., Skone, S., et al. (2013). Observations of global and regional ionospheric irregularities and scintillation using GNSS tracking networks. In *Proceedings of the ION 2013 Pacific PNT Meeting, Honolulu, HI* (pp. 752–761).

Pimenta, A. A., Sahai, Y., Bittencourt, J. A., & Rich, F. J. (2007). Ionospheric plasma blobs observed by OI 630 nm all-sky imaging in the Brazilian tropical sector during the major geomagnetic storm of April 6–7, 2000. *Geophysical Research Letters*, *34*(2), L02820. https://doi.org/10.1029/2006GL028529

Reinisch, B. W., Galkin, I. A., Khmyrov, G. M., Kozlov, A. V., Bibl, K., Lisysyan, I. A., et al. (2009). New Digisonde for research and monitoring applications. *Radio Science*, *44*(1), RS0A24. https://doi.org/10.1029/2008RS004115

Resende, L. C. A., Shi, J., Denardini, C. M., Batista, I. S., Picanço, G. A. S., Moro, J., et al. (2021). The impact of the disturbed electric field in the sporadic E (Es) layer development over Brazilian region. *Journal of Geophysical Research: Space Physics*, *126*(2), e2020JA028598. https://doi.org/10.1029/2020JA028598

Richmond, A. D., & Roble, R. G. (1997). Electrodynamic coupling effects in the thermosphere/ionosphere system. *Advances in Space Research*, *20*(6), 1115–1124. https://doi.org/10.1016/S0273-1177(97)00754-0

Scherliess, L., & Fejer, B. G. (1997). Storm time dependence of equatorial disturbance dynamo zonal electric fields. *Journal of Geophysical Research*, *102*(A11), 24037–24046. https://doi.org/10.1029/97JA02165

Seemala, G. K., & Valladares, C. E. (2011). Statistics of total electron content depletions observed over the South American continent for the year 2008. *Radio Science*, *46*(5), 1–14. https://doi.org/10.1029/2011RS004722

Silva, R. P., Souza, J. R., Sobral, J. H. A., Denardini, C. M., Borba, G. L., & Santos, M. A. F. (2019). Ionospheric plasma bubble zonal drift derived from total electron content measurements. *Radio Science*, *54*(7), 580–589. https://doi.org/10.1029/2018RS006727

Sripathi, S., Abdu, M. A., Patra, A. K., & Ghodpage, R. N. (2018). Unusual generation of localized EPB in the dawn sector triggered by a moderate geomagnetic storm. *Journal of Geophysical Research: Space Physics*, *123*(11), 9697–9710. https://doi.org/10.1029/2018JA025642

Su, Y.-J., Retterer, J. M., de La Beaujardière, O., Burke, W. J., Roddy, P. A., Pfaff, R. F., et al. (2009). Assimilative modeling of equatorial plasma depletions observed by C/NOFS. *Geophysical Research Letters*, *36*, L00C02. https://doi.org/10.1029/2009GL038946

Taieb, C., Scialom, G., & Kockarts, G. (1975). Daytime valley in the F1-region observed by incoherent scatter. *Planetary and Space Science*, *23*(3), 523–531. https://doi.org/10.1016/0032-0633(75)90122-1

Takahashi, H., Wrasse, C. M., Denardini, C. M., Pádua, M. B., de Páula, E. R., Costa, S. M. A., et al. (2016). Ionospheric TEC weather map over South America. *Space Weather*, *14*(11), 937–949. https://doi.org/10.1002/2016SW001474

Tulasi Ram, S., Ajith, K. K., Yamamoto, M., Otsuka, Y., Yokoyama, T., Niranjan, K., & Gurubaran, S. (2015). Fresh and evolutionary-type field-aligned irregularities generated near sunrise terminator due to overshielding electric fields. *Journal of Geophysical Research: Space Physics*, *120*(7), 5922–5930. https://doi.org/10.1002/2015JA021427

Vargas, F., Brum, C., Terra, P., & Gobbi, D. (2020). Mean zonal drift velocities of plasma bubbles estimated from keograms of nightglow all-sky images from the Brazilian sector. *Atmosphere*, *11*(1), 69. https://doi.org/10.3390/atmos11010069

Venkatesh, K., Tulasi Ram, S., Fagundes, P. R., Seemala, G. K., & Batista, I. S. (2017). Electrodynamic disturbances in the Brazilian equatorial and low-latitude ionosphere on St. Patrick's Day storm of 17 March 2015. *Journal of Geophysical Research: Space Physics*, *122*(4), 4553–4570. https://doi.org/10.1002/2017JA024009

Verkhoglyadova, O. P., Tsurutani, B. T., Mannucci, A. J., Mlynczak, M. G., Hunt, L. A., Paxton, L. J., & Komjathy, A. (2016). Solar wind driving of ionosphere-thermosphere responses in three storms near St. Patrick's Day in 2012, 2013 and 2015. *Journal of Geophysical Research: Space Physics*, *120*(9), 8900–8923. https://doi.org/10.1002/2016JA022883

Weimer, D. R. (2005). Improved ionospheric electrodynamic models and application to calculating Joule heating rates. *Journal of Geophysical Research*, *110*(A5), A05306. https://doi.org/10.1029/2004JA010884

Wolf, R. A. (1995). Magnetospheric configuration. In M. G. Kivelson & C. T. Rusell (Eds.), *Introduction to space physics* (pp. 288–329). Cambridge University Press.

Wu, K., Xu, J., Yue, X., Xiong, C., Wang, W., Yuan, W., et al. (2020). Equatorial plasma bubbles developing around sunrise observed by an all-sky imager and global navigation satellite system network during storm time. *Annales Geophysicae*, *38*(1), 163–177. https://doi.org/10.5194/angeo-38-163-2020

Yeh, H. C., Su, S. Y., & Heelis, R. A. (2001). Storm time plasma irregularities in the pre-dawn hours observed by the low-latitude ROCSAT-1 satellite at 600 km altitude. *Geophysical Research Letters*, *28*(4), 685–688. https://doi.org/10.1029/2000GL012183

Yokoyama, T., Shinagawa, H., & Jin, H. (2015). Nonlinear growth, bifurcation and pinching of equatorial plasma bubble simulated by three-dimensional high-resolution bubble model. *Journal of Geophysical Research: Space Physics*, *119*(12), 10474–10482. https://doi.org/10.1002/2014JA020708

Zakharenkova, I., Cherniak, I., & Krankowski, A. (2019). Features of storm-induced ionospheric irregularities from ground-based and spaceborne GPS observations during the 2015 St. Patrick's Day Storm. *Journal of Geophysical Research: Space Physics*, *124*(12), 10728–10748. https://doi.org/10.1029/2019JA026782

Zalesak, S. T., Ossakow, S. L., & Chaturvedi, P. K. (1982). Nonlinear equatorial spread F: The effect of neutral winds and background Pedersen conductivity. *Journal of Geophysical Research: Space Physics*, *87*(A1), 151–166. https://doi.org/10.1029/JA087iA01p00151

Zhang, S.-R., Zhang, Y., Wang, W., & Verkhoglyadova, O. P. (2017). Geospace system responses to the St. Patrick's Day storms in 2013 and 2015. *Journal of Geophysical Research: Space Physics*, *122*(6), 6901–6906. https://doi.org/10.1002/2017JA024232